

DUST GRAIN GROWTH & DUSTY SUPERNOVAE IN LOW-METALLICITY MOLECULAR CLOUDS

SERGIO MARTÍNEZ-GONZÁLEZ¹, RICHARD WÜNSCH², GUILLERMO TENORIO-TAGLE³, SERGIY SILICH³, DOROTTYA SZÉCSI^{4,5},
JAN PALOÚŠ²

ACCEPTED BY APJ: June 11th, 2022.

Abstract

We present 3-D hydrodynamical models of the evolution of superbubbles powered by stellar winds and supernovae from young coeval massive star clusters within low metallicity ($Z = 0.02 Z_{\odot}$), clumpy molecular clouds. We explore the initial stages of the superbubble evolution, including the occurrence of pair-instability and core-collapse supernovae. Our aim is to study the occurrence of dust grain growth within orbiting dusty clumps, and in the superbubble's swept-up supershell. We also aim to address the survival of dust grains produced by sequential supernovae. The model accounts for the star cluster gravitational potential and self-gravity of the parent cloud. It also considers radiative cooling (including that induced by dust) and a state-of-the-art population synthesis model for the coeval cluster. As shown before, a superbubble embedded into a clumpy medium becomes highly distorted, expanding mostly due to the hot gas streaming through low density channels. Our results indicate that in the case of massive ($\sim 10^7 M_{\odot}$) molecular clouds, hosting a super star cluster ($\sim 5.6 \times 10^5 M_{\odot}$), grain growth increments the dust mass at a rate $\sim 4.8 \times 10^{-5} M_{\odot} \text{ yr}^{-1}$ during the first 2.5 Myr of the superbubble's evolution, while the net contribution of pair-instability and core-collapse supernovae to the superbubble's dust budget is $\sim 1200 M_{\odot} (M_{SC}/5.6 \times 10^5 M_{\odot})$, where M_{SC} is the stellar mass of the starburst. Therefore, dust grain growth and dust injection by supernovae lead to create, without invoking a top-heavy initial mass function, massive amounts of dust within low-metallicity star-forming molecular clouds, in accordance with the large dust mass present in galaxies soon after the onset of cosmic reionization.

Keywords: galaxies: star clusters: general — (ISM:) dust, extinction — Physical Data and Processes: hydrodynamics

1. INTRODUCTION

Most massive stars reside within young massive star clusters (Lada & Lada 2003; Portegies Zwart et al. 2010). There, hundreds to thousands of massive stars inject large amounts of metal-enriched gas via stellar winds and supernova explosions. Consequently, a localized dust enrichment of galaxies originating from massive star clusters can be expected Consiglio et al. (2016). An important amount of this dust is likely produced after the efficient condensation of the ejecta of core-collapse supernovae (e.g. Todini & Ferrara 2001; Indebetouw et al. 2014, and references therein) and pair-instability supernovae (PISNe, Nozawa et al. 2003; Cherkneff 2010). A competing mechanism that may massively enhance the amount of dust is the accretion of gas species onto already existing dust grains (Dwek 1998; Zhukovska et al. 2008; Asano et al. 2013; Calura et al. 2008, 2014). Both processes, dust produced by supernovae and dust grain growth, are expected to play an important role in local and high-redshift galaxies. For instance, Gall & Hjorth (2018) concluded that the amount of dust observed in

high-redshift galaxies comes from an efficient supernova dust production, followed by a rapid dust grain reformation if dust is destroyed by high-velocity shocks (see also Priestley et al. 2021). Observations of Ly α systems and quasar host galaxies at high redshifts suggest a rapid transition (on the order of a few Myr) from having a dust-poor to a dust-rich interstellar medium (e.g. Michałowski et al. 2010; Mattsson et al. 2015), particularly if star formation took place with a top-heavy initial mass function (Gall et al. 2011; Dwek & Cherkneff 2011). It is also worth mentioning that the cold envelopes of the most massive AGB stars could also be important dust producers at high-redshifts (e.g. Valiante et al. 2009; Leńniewska & Michałowski 2019). Moreover, dust formation from early-type carbon-rich Wolf-Rayet binaries could also represent an important source of dust in low-metallicity environments ($Z \leq 0.65 Z_{\odot}$ Lau et al. 2021). The three-dimensional hydrodynamical evolution of dusty supernova remnants originating within young massive stellar clusters was explored in Martínez-González et al. (2018). For that purpose, CINDER (COOLING INDUCED BY DUST & EROSION RATES), a module for the adaptive mesh refinement code FLASH (Fryxell et al. 2000), was developed. With CINDER one can follow the survival rate of dust condensed out of a supernova ejecta and subjected to multiple shock processing, that includes the passage of the reverse shock and its bouncing back, the interaction with shocked stellar winds and the crossing of sequential supernova forward shocks. In the case of off-centered supernova remnants, facing a steep density gradient, a blowout phase is triggered: the superno-

¹ CONACYT-Instituto Nacional de Astrofísica, Óptica y Electrónica, AP 51, 72000 Puebla, México: sergiomtz@inaoep.mx

² Astronomical Institute, Czech Academy of Sciences, Boční II 1401/1, 141 00 Praha 4, Czech Republic

³ Instituto Nacional de Astrofísica, Óptica y Electrónica, AP 51, 72000 Puebla, México

⁴ I. Physikalisches Institut, Universität zu Köln, Zùlpicher Strasse 77, D-50937 Köln, Germany

⁵ Institute of Astronomy, Faculty of Physics, Astronomy and Informatics, Nicolaus Copernicus University, Grudziądzka 5, 87-100 Toruń, Poland

va remnants elongate in preferential directions, become Rayleigh–Taylor unstable and the supernova ejecta suffers a rapid decline in density and temperature (Tenorio-Tagle et al. 2015; Jiménez et al. 2021). The main result of the “pyroclastic blowout model” is that clustered supernova explosions are likely to cause a net increase in the amount of dust in the free wind region surrounding their parental stellar clusters.

However, the mechanical feedback provided by the cluster leads to the creation of a wind-blown superbubble (see Weaver et al. 1977; Mac Low & McCray 1988; Koo & McKee 1992; Bisnovatyi-Kogan & Silich 1995), where a supershell of swept-up interstellar matter encompasses the hot and tenuous free/shocked wind region. Thus, one cannot exclude that supernova remnants originating from the star cluster overrun the free and shocked wind regions, to then impact directly the swept-up supershell. This results in a further processing of both, the ejecta dust and the dust grains present in the supershell. Furthermore, supershells represent a fertile environment for the growth of dust grains even in high-redshift ($z \sim 6$) galaxies at supersolar metallicities (Martínez-González et al. 2021).

The collision of supernova remnants with a wind-driven shell has been previously explored (Tenorio-Tagle et al. 1990, 1991; Franco et al. 1991; Różyczka et al. 1993; Dwarkadas 2005, 2007; van Marle et al. 2015; Haid et al. 2016). In Martínez-González et al. (2019), it has been shown that the pre-existent dust locked-up in a wind-driven shell is mostly not in danger of being significantly destroyed after the collision of blast waves with the surrounding shell. This is expected as blast waves would transmit weakly into the much denser encompassing shell.

In the present work, we extend the models presented in (Martínez-González et al. 2018, 2019, hereafter referred as Papers I and II), and follow the wind-blown superbubble evolution in the context of low-metallicity clumpy molecular clouds. Those low-metallicity environments may be representative of the Green Pea galaxies, a local analog class of high redshift Ly α emitting galaxies with a high star formation rate (Cardamone et al. 2009; Micheva et al. 2017; Svoboda et al. 2019; Franek et al. 2021). They are also interesting since an increased pre-supernova feedback (harder ionizing radiation and increased photon fluxes) is expected in low-metallicity environments (*e.g.* McLeod et al. 2021). We will consider the potential well of the molecular cloud and the star cluster, the growth of grains originally residing within clumps, as well as dust grains produced in multiple pair-instability and core-collapse supernova explosions.

The Paper is organized as follows: In Section 2 we describe the characteristics of the host molecular cloud (2.1), the central star cluster and the wind-driven superbubble (2.2), the growth of dust grains (2.3), and the occurrence of supernovae (2.4). In Sections 3-5, we present the results of the hydrodynamical simulations regarding the early evolution of the superbubble, and the dust mass evolution. In Section 6 we highlight the limitations of our model. Finally, in Section 7 we summarize our results and present the main conclusions.

2. MODEL

2.1. Clumpy Molecular Cloud

We have modelled a hierarchical molecular cloud consisting of a collection of small clumps and a tenuous interclump envelope (Tenorio-Tagle et al. 2006; Draine 2011). It is assumed that the cloud’s metallicity is $Z = 0.02 Z_{\odot}$, and that the cloud’s clumpy density field is determined by (Reynolds et al. 2019)

$$\rho_{cl}(\mathbf{x}) = \rho_0 \left(1 + \sum_{i=1}^{n_{cl}} \frac{\rho_i}{\rho_0} e^{-2(\|\mathbf{x}-\mathbf{x}_i\|/r_i)^2} \right), \quad (1)$$

where $\mathbf{x} = (x, y, z)$, ρ_0 is the interclump gas mass density, n_{cl} is the number of clumps, ρ_i and r_i are the mass density and radius of the i th spherical clump centered at $\mathbf{x}_i = (x_i, y_i, z_i)$. Hereafter, we assume that $n_{cl} = 1000$ and adopt for the interclump gas density $\rho_0 = 2.128 \times 10^{-22} \text{ g cm}^{-3}$, with a mean mass per ion $1.22m_H$, and a mean mass per molecular gas $2.33m_H$, where m_H is the proton mass.

Each clump is initially assumed to have a turbulent velocity field, as implemented by Taylor et al. (2018). The clumps’ kinetic energy spectra take the form $E(k) \propto k^{\alpha}$, with wavenumbers k between $2 \times 2\pi/L$ and $32 \times 2\pi/L$, where L is the length of the computational domain, and $\alpha = -5/3$. The virial ratio of the clumps is assumed to be 0.9. We have taken normally-distributed values of x_i , y_i , z_i , ρ_i/ρ_0 and r_i . The mean and standard deviation of x_i , y_i , and z_i are 0 pc and 20 pc. For ρ_i/ρ_0 they are 66 and 50, respectively. For r_i these are 1.0 pc and 0.76 pc, respectively. The clumps amount to $M_{cl} \sim 3.73 \times 10^6 M_{\odot}$ of molecular gas (roughly one third of the total gas mass $\sim 1.03 \times 10^7 M_{\odot}$), with ~ 68 per cent of the clumps located within 13 pc.

2.2. The Star Cluster & the Wind-driven Superbubble

We have set-up the three-dimensional hydrodynamical evolution of a superbubble within a molecular cloud with the characteristics described in Section 2.1 (see Table 1), using a similar setup to that described in Papers I and II. The superbubble is driven by the mechanical feedback of a coeval young massive stellar cluster located at the cloud’s center. To this end, we have used the adaptive mesh refinement code FLASH v4.3 (Fryxell et al. 2000). The employed hydrodynamical solver is a modified version of the Piecewise Parabolic Method introduced by Colella & Woodward (1984). Similarly to Paper I, the simulations take into account the star cluster’s gravitational potential and the self-gravity of the gas calculated by the tree-based solver developed by Wünsch et al. (2018), and the optically thin cooling function for gas at temperatures $T \geq 10^4 \text{ K}$ (Schure et al. 2009), and for gas at temperatures $T < 10^4 \text{ K}$, gas cooling due to radiation emitted from hydrogen-deuteride ground-state rotational transition Dalgarno & McCray (1972). We have used CINDER (Martínez-González et al. 2018, 2019) to follow the injection and destruction of dust grains due to thermal sputtering, as well as the cooling induced by gas-grain collisions in hot plasmas ($T \gtrsim 10^5 \text{ K}$). As in Papers I and II, we have not included other grain destruction mechanisms such as kinetic sputtering and grain shattering (see subsection 6). Additionally, the process of dust grain growth is incorporated into CINDER for the first time.

Table 1
THE HOST MOLECULAR CLOUD & THE STAR CLUSTER

Model	M_{MC} M_{\odot}	Z Z_{\odot}	n_{cl} –	ρ_0 g cm^{-3}	M_{SC} M_{\odot}	R_{ch} pc	R_{SC} pc	ϵ per cent	No. Stars $\geq 71 M_{\odot}$	Grain Growth –	Ejecta dust –
GRAINGROWTH	10^7	0.02	1000	2.26×10^{-22}	5.6×10^5	1.0	3.0	3.7	186	Yes	No
SNDUST	10^7	0.02	1000	2.26×10^{-22}	5.6×10^5	1.0	3.0	3.7	186	No	Yes

Note. — The Table summarizes the main properties of the host molecular cloud (mass, metallicity, number of molecular clumps and the interclump mass density), and the star cluster (stellar mass, the stellar distribution’s characteristic scale and cut-off radii, the global star formation efficiency, and number of progenitor stars that end as PISNe). The last two columns indicate whether the processes of dust grain growth and dust injection by supernovae are considered.

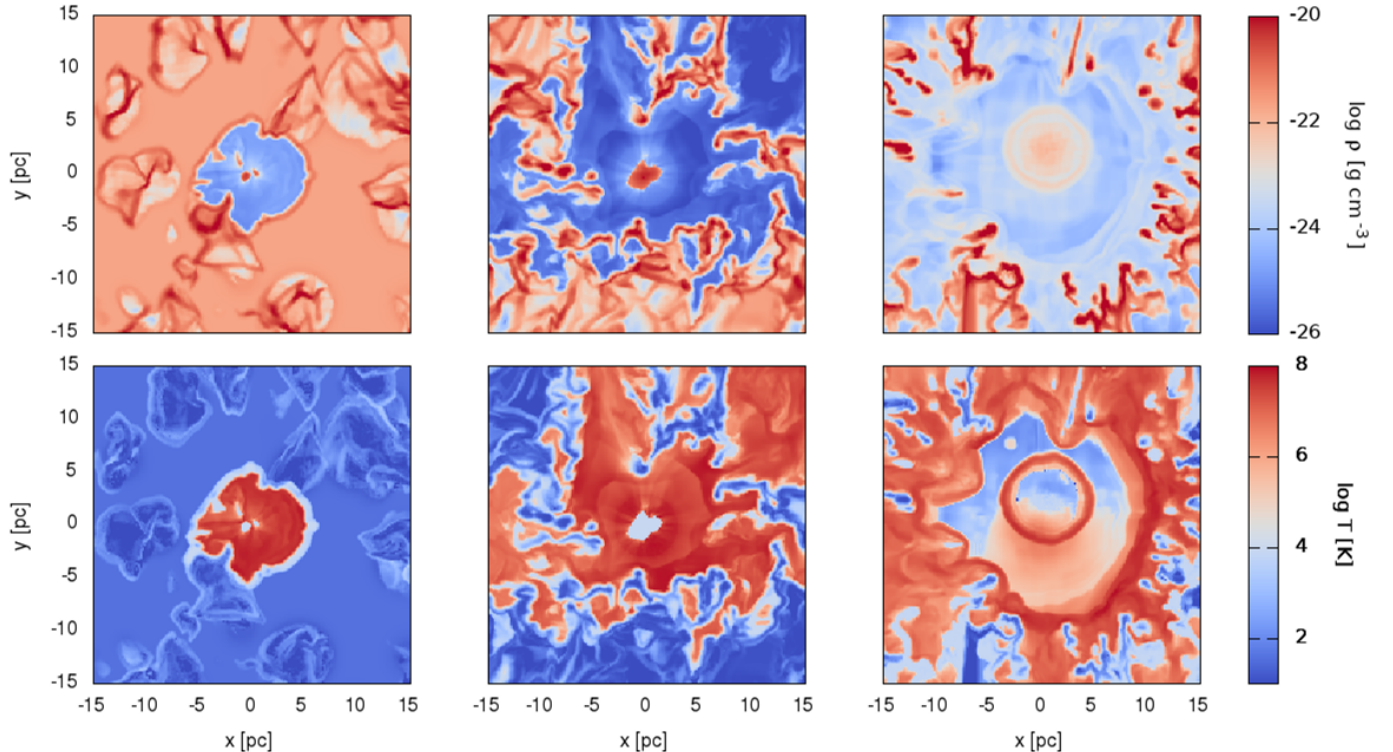


Figure 1. The stream of hot gas through low-density channels. The upper and bottom panels display slides in the z -plane of the distribution of gas mass density and gas temperature, respectively, at three different times (left: 100 kyr; center: 2.0 Myr; right: 2.65 Myr). The flow of thermalized matter between low-temperature overdensities leads first to the distortion of the starburst-driven shell, and then to the development of multiple ragged shells at later times. Note the left and central panels correspond to model GRAINGROWTH, while the right panels depict model SNDUST, once PISNe are occurring and the superbubble’s interior is filled with wind and supernova matter. At 2.65 Myr, a young supernova remnant can be identified as a ring-like hot structure exhibiting its forward and reverse shocks, and surrounded by the free-wind region with a density that falls as $\sim r^{-2}$. Further out, there is a global reverse shock thermalizing the free cluster wind and causing a temperature larger than 10^7 K (appearing as a red zone at ~ 10 pc from the center). Much further out there is a leading shock that has managed to display the original fragments from the central regions, while advancing with different speeds in different directions given the uneven density left in the surrounding medium.

The simulations are inscribed into cubes $(40 \text{ pc})^3$ and $(140 \text{ pc})^3$ (when indicated) in a grid 256^3 in Cartesian geometry, with outer boundary conditions set to outflow. We follow the evolution of the star cluster wind mechanical output, mass-loss rate and terminal speed using the BOOST stellar model grids and the SYNSTARS stellar population synthesis code (Szécsi et al. 2020; Franek et al. 2021). In particular, we rely on a stellar grid with metallicity $0.02 Z_{\odot}$ (originally presented by Szécsi et al. 2015), which consists of slowly rotating single stars computed with the ‘Bonn’ stellar evolution code with standard wind mass-loss prescriptions (Vink et al. (2000, 2001) type mass loss in the OB phase and Nieuwen-

huijzen & de Jager (1990) mass loss in the supergiant phase). As discussed by Szécsi & Wunsch (2019), these models spend their main-sequence lifetimes as hot OB stars, and their post-main-sequence as cool supergiants; none of them form Wolf–Rayet stars, as the metallicity is too low for the self-stripping by the wind. The stellar winds of these massive stars do contribute to the mechanical energy inserted into the cluster, but neither the wind yields, nor the supernova yields from these models are included into the 3–D hydrodynamical simulations. We apply a Kroupa initial stellar mass function (IMF) in the mass interval $[0.01\text{--}120] M_{\odot}$. The adopted stellar

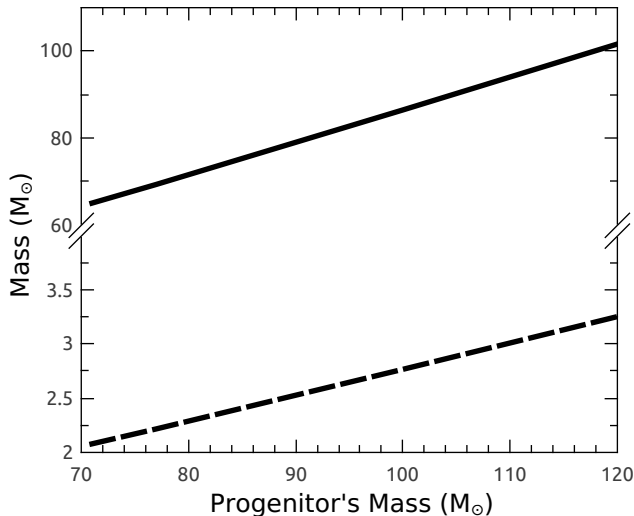


Figure 2. The plot shows the ejecta mass (solid line) and the assumed ejecta-condensed dust mass (dashed line) as functions of the progenitor’s mass (measured at the zero-age main-sequence). The mass of the ejecta corresponds to the progenitor’s final mass, and the ejecta-condensed dust mass is assumed to be 3.2 per cent of the ejecta mass¹ (Cherchneff 2010). mass¹ is $5.6 \times 10^5 M_{\odot}$, distributed according to a Schuster stellar density profile $\rho_{\star} \propto [1 + (r/R_{ch})^2]^{-\beta}$ with characteristic scale radius $R_{ch} = 1$ pc, cut-off radius $R_{SC} = 3$ pc and index $\beta=1.5$ (Palouš et al. 2013; Martínez-González et al. 2016, 2017). The global star formation efficiency is $\epsilon = M_{SC}/M_{MC} = 3.7$ per cent.

2.3. Dust Grain Growth

We have incorporated the process of dust grain growth via the accretion of gas species (Spitzer 1978), so individual dust grains increase their mass at a rate $\dot{m}_{gr} = 3m_{gr}\dot{a}/a$, where m_{gr} is the grain mass and \dot{a} is the rate of increase in their radius a . Similarly to Paper II, we consider graphite and silicate dust grains and a log-normal grain size distribution of the form $\sim a^{-1} \exp\{-0.5[\log(a/a_0)/\sigma]^2\}$; with $a_0 = 0.1 \mu\text{m}$ and $\sigma = 0.7$ and minimum and maximum grain sizes $a_{min} = 5$ nm and $a_{max} = 0.5 \mu\text{m}$, respectively. The grain size distribution is sampled by 10, logarithmically-spaced, size bins. The dust-to-gas mass ratio, $\mathcal{D}^{(i)}$, in a bin with representative grain size, $a_m^{(i)}$, at time $t + \Delta t$ is (Valentini & Brighenti 2015)

$$\mathcal{D}^{(i)}(t + \Delta t) = \mathcal{D}^{(i)}(t) \left(1 + \frac{3|\dot{a}|\Delta t}{a_m^{(i)}} \right), \quad (2)$$

where \dot{a} is given by

$$\dot{a} = \frac{f_{gr}\rho_r S}{4\rho_{gr}} \left[f_{M_d}^{(i)} \mathcal{D}^{max} - \mathcal{D}^{(i)} \right] \left(\frac{8k_B T}{\pi\mu_r} \right)^{1/2}. \quad (3)$$

In equation (3) ρ_r is the local refractory gas mass density, ρ_{gr} is the grain’s bulk density, S is the sticking coefficient, f_{gr} is the fraction of grain species (for simplicity

¹ This value is inspired by the derived mass of NGC 604 (Relaño et al. 2016). As we shall see, the simulated star cluster, superbubble and molecular cloud resemble the complex morphology of massive HII regions such as NGC 604.

f_{gr} is set to 0.5 for both graphite and silicate grains), $f_{M_d}^{(i)}$ is the initial dust mass fraction of the i th grain size, k_B and $\mu_r = 18.11m_H$ are the Boltzmann constant and the mean mass per refractory atom (*i.e.* excluding non-condensable gas species). $\mathcal{D}^{max} = 2.1 \times 10^{-4}$ is the dust-to-gas mass ratio in the case all refractory elements are locked-up onto dust grains. This value is taken from the initial mass fractions of refractory elements in the ‘Bonn’ stellar evolution code. At the explored molecular gas metallicity ($Z = 0.02 Z_{\odot}$), refractory elements make up a gas mass fraction of $\lesssim 10^{-6}$, a quantity that is well approximated by the relation $\mathcal{D}^{max} \approx 10^{-2} \times Z$ (Martínez-González et al. 2021).

We allow dust grain growth to occur at gas temperatures $T \leq 1000$ K (Nozawa et al. 2012). At these temperatures, grains with radius ≥ 5 nm embedded into a gas with molecular gas mass density $\leq 10^5 \text{ cm}^{-3}$ have an equilibrium temperature ≤ 30 K. Consequently, the grain sticking coefficient S is approximated as 1.0 (Ferrara et al. 2016).

2.4. Supernovae

At their oxygen-burning phase, massive CO stellar cores ($\gtrsim 65 M_{\odot}$) undergo the so-called electron-positron pair-creation instability (Fowler & Hoyle 1964). This leads to the disruption of the whole star as a PISN, leaving behind neither a black hole, nor a neutron star (Kozyreva et al. 2014, and references therein). According to the BoOST low-metallicity stellar tracks, that occurs for stars with masses $\gtrsim 71 M_{\odot}$ at the zero-age main-sequence. From the assumed IMF, we thus follow the occurrence of 186 PISNe between 2.55 and 3.18 Myr. The supernova rate is a function of the star cluster mass, the IMF, and the metallicity of the parent cloud, and thus evolves with time. We, however, have set a constant supernova rate for progenitors in the mass intervals [71–80] M_{\odot} , [80–90] M_{\odot} , [90–100] M_{\odot} , [100–110] M_{\odot} , and [110–120] M_{\odot} , with one supernova per 4250 years, 3300 years, 3050 years, 2880 years, and 2460 years, respectively. Supernovae are randomly-distributed following the assumed stellar density profile. As PISNe completely obliterate their progenitor stars, their ejecta masses, M_{ej} , correspond to the final masses obtained from the BoOST stellar model grids. With respect to the total energy released in a single PISN event, we assume $E_{SN} = 5 \times 10^{51}$ erg. This energy is inserted into a sphere of radius equivalent to five grid-cells. Massive stars with final masses $\sim [10\text{--}65] M_{\odot}$ explode as core-collapse supernovae (Szécsi et al. 2020). We have thus explored the occurrence of the first 50 core-collapse supernovae starting after the last PISNe. Our assumption is that each core-collapse supernova releases $M_{ej} = 10 M_{\odot}$ of gas and $E_{SN} = 10^{51}$ erg in the form of kinetic energy. For each supernova, the initial ejecta gas mass density distribution is assumed to be given by

$$\rho_{ej} = \frac{(3 - \omega)}{4\pi} \frac{M_{ej}}{R_{SN}^3} \left(\frac{R_{SN}}{r'} \right)^{\omega}, \quad (4)$$

where r' is the radial distance from the center of the explosion and $\omega = 5/2$ was set for all supernovae. The initial ejecta velocity distribution is assumed to be

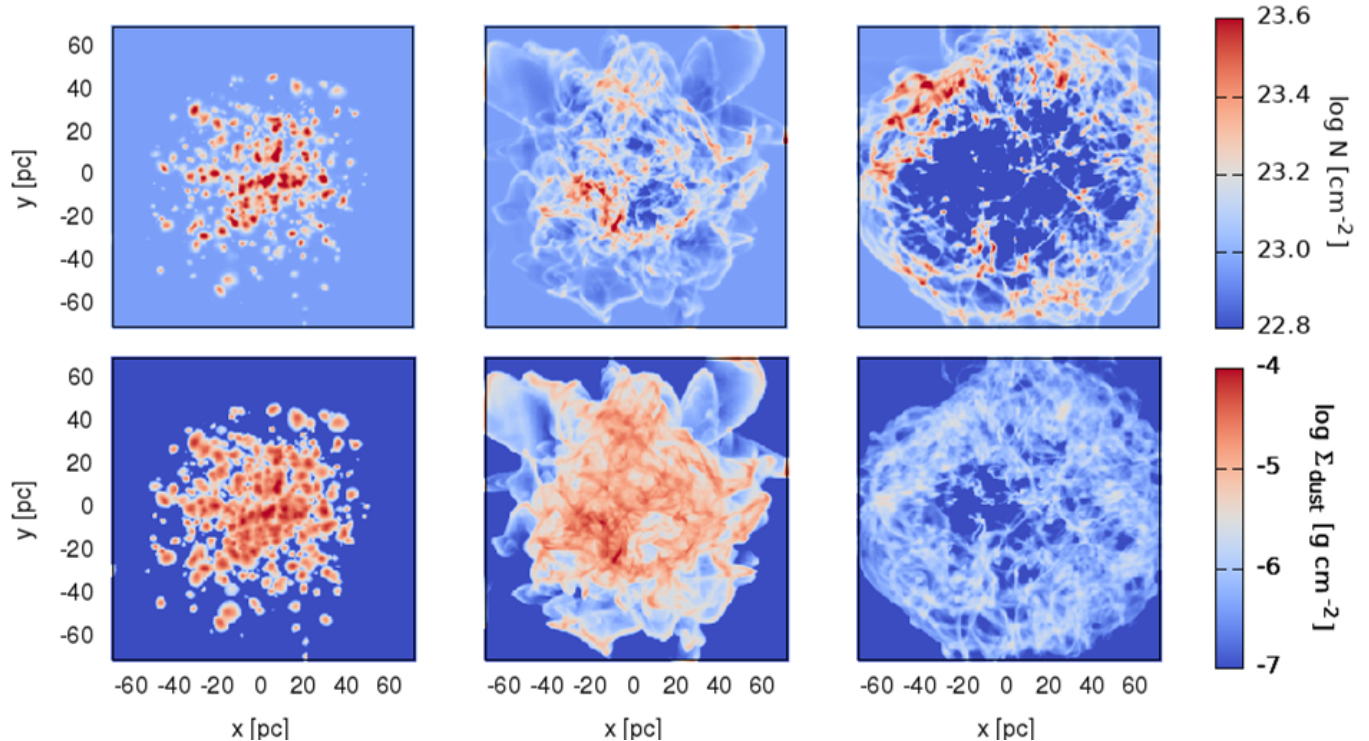


Figure 3. The wind-blown superbubble’s evolution in an initially clumpy medium. The central star cluster has a mass $5.6 \times 10^5 M_{\odot}$. The upper, and bottom panels show the gas column density, and the dust mass surface density (model GRAINGROWTH), respectively. The left and central and right panels correspond to three different evolutionary times (left: 100 kyr, center: 2.5 Myr, for model GRAINGROWTH; right: 3.2 Myr for model SNDUST). Soon, the host molecular cloud and the superbubble acquire complex morphologies due to the action of gravity and the flow of hot gas through channels between clumps/filaments. An animated version of this Figure can be found on Github.

$$v_{ej} = \left(2 \frac{(5 - \omega) E_{SN}}{(3 - \omega) M_{ej}} \right)^{1/2} \left(\frac{r'}{R_{SN}} \right). \quad (5)$$

3. LARGE-SCALE EVOLUTION

In our first model GRAINGROWTH, we follow the occurrence of dust grain growth during the evolution of the molecular cloud and the superbubble driven by the central star cluster. Given the low gas temperatures involved in the host molecular cloud, and hence short cooling timescales and small cooling lengths, we have modelled the central $(40 \text{ pc})^3$ at three spatial resolutions, 0.15 pc and 0.31 pc, respectively. Additionally, we tested the results with a larger computational domain, $(140 \text{ pc})^3$ at a resolution 0.54 pc, which encompasses all the molecular clumps. In this model we initially assume that half the mass of refractory elements within molecular clumps are already depleted onto dust grains, so that their dust-to-gas mass ratio is $\mathcal{D} = \frac{1}{2} \mathcal{D}^{max}$ (and zero elsewhere). Thus the initial dust mass within molecular clumps is $\frac{1}{2} \mathcal{D}^{max} M_{cl} \approx 373 M_{\odot}$. The initial population of dust grains is assumed to have been originated in prior (very early) generations of supernovae (Nozawa et al. 2012). We stop our calculations just before the occurrence of the first PISNe.

As the molecular cloud evolution proceeds, clumps become elongated and end up forming filamentary structures while they revolve around the gravitational potential well. We note that the potential well is dominated by the

molecular gas, rather than the central star cluster. During the process, the clumps interact, collide and coalesce with other clumps (Elmegreen 1988). The superbubble thus expands preferentially along the paths of least resistance, *i.e.* through the lower density channels between clumps/filaments (Tenorio-Tagle et al. 2006; Alúzar et al. 2012; Rogers & Pittard 2013; Lucas et al. 2020; Lancaster et al. 2021a,b, see Figure 1).

The end result is that the superbubble morphology becomes highly distorted. The flow of thermalized matter between clumps/filaments leads first to the distortion of the star cluster wind-driven shell (displayed in the bottom panels of Figure 1 by the blue/cool contours encompassing the red/hot zones) and then to the development of multiple shells, some of them appearing as nested shells when they are seen projected against the background (see Figures 2 and 3 in Tenorio-Tagle et al. 2006). Those multiple shells are all interconnected, thus forming a large-scale supershell. Eventually, the superbubble, powered mostly by the SN shocks, will breakout/blowout from the host molecular cloud (Tenorio-Tagle 2002); however this moment is not captured in our simulations within our computational domain.

The top and bottom panels in Figure 3 present the evolution of the gas column density, N , and dust mass surface density, Σ_{dust} , integrated along the line-of-sight at 100 kyr and 2.5 Myr for model GRAINGROWTH. The right panels in the Figure correspond to 3.2 Myr in the case of model SNDUST, so Σ_{dust} corresponds to supernova-condensed dust only.

4. DUST GRAIN GROWTH AT LOW METALLICITY

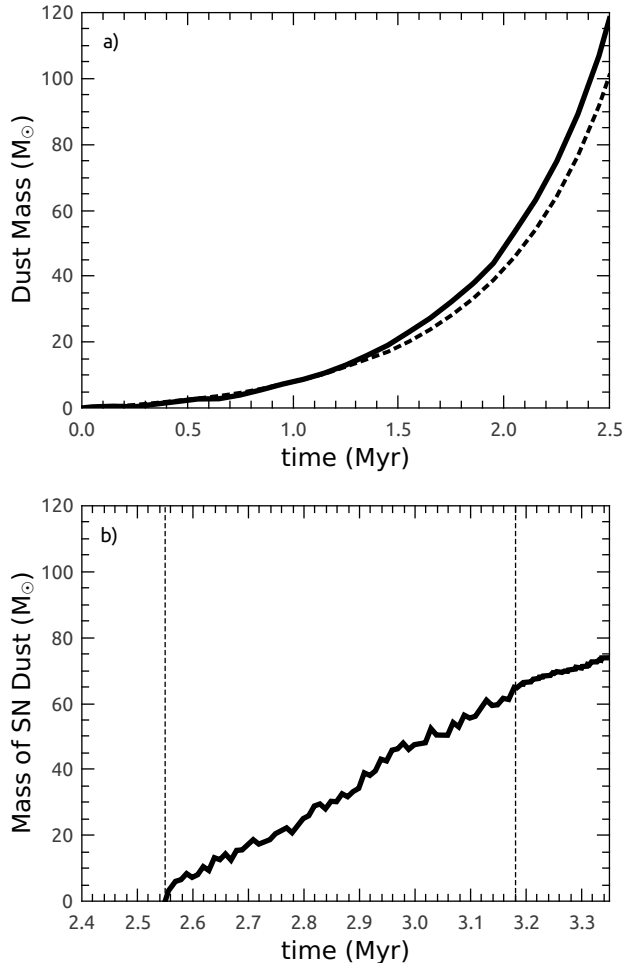


Figure 4. The dust mass evolution. Panel *a* presents the increment of dust mass due to grain growth in the central part (40^3 pc^3) of the molecular cloud/supershell during the pre-supernova era (model GRAINGROWTH). The thick line depicts the result of the run with the 0.15 pc spatial resolution, while the dashed line to the 0.31 pc spatial resolution run. Panel *b* displays the cumulative ejecta-condensed dust mass deposited by PISNe. The vertical dashed lines in panel *b* mark the onset and finale of the PISN era. Note the different time intervals depicted in both panels.

In model GRAINGROWTH, dust grain growth is promoted when the molecular clumps become filamentary and mix with the interclump material. It is also favoured when interclump gas is incorporated into the dense shells formed as the hot gas streams through low-density channels. We note that as the shells cool down quickly, a negligible amount of swept-up dust is destroyed. As a result, the dust mass increases at a rate $\sim 4.8 \times 10^{-5} M_{\odot} \text{ yr}^{-1}$, leading to a net increase of $\sim 120 M_{\odot}$ within 2.5 Myr (see panel *a* in Figure 4). The results with resolutions 0.31 pc and 0.54 pc show a reduction of 13 and 25 per cent, respectively, on the amount of dust grain growth. This is expected since decreasing the resolution inhibits efficient mixing of dust-free and dust-rich gas via numerical viscosity.

As we have set the outer boundary conditions to outflow, there is some fraction of the dust mass that leaves the computational domains. However, the majority of the

gas/dust overdensities remain within the central part of the molecular cloud.

We note that if dust-induced cooling of molecular gas were at play (not included in the current version of CINDER), the shells would be much thinner, denser and much colder, and thus they may promote a much more efficient growth of dust grains at higher gas metallicities (Martínez-González et al. 2021). Higher resolution simulations are required in such a case.

5. DUST INJECTED BY SUPERNOVAE

Model SNDUST explores the injection of dust by sequential PISN and core-collapse supernovae, while molecular clumps are set to be dust-free (*i.e.* no grain growth occurs). This model is studied at a resolution 0.54 pc since the cooling length² in the cavity is very large due to its low density and high temperature.

It is assumed that each PISNe leads to the condensation of 3.2 per cent of the progenitor’s final mass (around $3.25 M_{\odot}$ for a $120 M_{\odot}$ progenitor star) onto dust grains (see Figure 2). Such high value is consistent with theoretical expectations for dust condensation in PISNe occurring from zero-metallicity progenitors (Cherchneff 2010). The dust mass condensed out of supernova ejecta for core-collapse supernovae is assumed as normally-distributed, with a mean of $0.6 M_{\odot}$ and standard deviation of $0.1 M_{\odot}$. Similarly to the grains originally locked-up within molecular clumps, the simulated supernovae are also assumed to inject graphites and silicates in equal mass fractions following a log-normal grain size distribution. We have not included the process of ion trapping onto dust grains (see Kirchsclager et al. 2020), although such a process can produce a further growth of ejecta-condensed dust grains.

Panel *b* in Figure 4 shows that, despite the occurrence of several PISN explosions, the amount of ejecta-condensed dust increments steadily, at a rate $10^{-4} M_{\odot} \text{ yr}^{-1}$ between 2.55 and 3.18 Myr. To put it into perspective, we find that from $470 M_{\odot}$ of ejecta dust that were injected during the era of PISNe, about 13 per cent ($\sim 61 M_{\odot}$) remains in the superbubble’s cavity $\sim 320 \text{ kyr}$ after the last PISN. This value is in agreement with the conclusions raised in Paper I, that explored, at a higher resolution ($\sim 0.11 \text{ pc}$), the case of sequential core-collapse supernova explosions, occurring at a similar rate, within a star cluster wind. It also builds on the conclusion that massive shells represent insurmountable barriers that protect the vast majority of the pre-existing surrounding dust from being shock-processed (Paper II).

Progenitors with final masses $\sim [10\text{--}65] M_{\odot}$ explode as core-collapse supernovae. We have found that from the $\sim 30 M_{\odot}$ of ejecta dust that were injected into the simulation, ~ 32 per cent ($\sim 9.5 M_{\odot}$) survives after 175,000 years from the first core-collapse supernova explosion. If we extrapolate the rate of net dust injection by core-collapse supernovae until $\sim 21 \text{ Myr}$ of the cluster’s evolution (the time needed to explode a $10 M_{\odot}$ star in the BOOST low-metallicity stellar tracks), we can expect a net increase in the dust mass by $\sim 1200 M_{\odot} (M_{SC}/5.6 \times 10^5 M_{\odot})$. Applying this estimate to the gravitationally-

² The cooling length can be defined as the product of the local sound speed and the cooling time, and increases with decreasing gas density and metallicity (Smith et al. 2017).

lensed galaxy A2744_YD4 (at a redshift $z \sim 8.38$, Laporte et al. 2017), with a total stellar mass $\sim 2 \times 10^9 M_\odot$, we obtain a net dust contribution by supernovae $\sim 4.3 \times 10^6 M_\odot$. This value fits pretty well the dust mass ($6 \times 10^6 M_\odot$) derived by Laporte et al. (2017) (see also Behrens et al. 2018). Note that our estimate relies on a standard Kroupa initial stellar mass function, *i.e.* a top-heavy IMF was not necessary in order to explain such a large dust mass produced by pair-instability and core-collapse supernovae. We have also tested the occurrence of the first five PISNe at a resolution 0.15 pc in a domain $(40 \text{ pc})^3$ (see the right panels in Figure 1), and the results agree within 15 per cent.

6. RADIATIVE HEATING, INTERSTELLAR MAGNETIC FIELD, & GAS-DUST COUPLING

Radiative heating provided by the central stellar cluster is not included into the simulations. We have, however, set a standard heating rate $2 \times 10^{-26} \text{ erg s}^{-1}$ (Koyama & Inutsuka 2002). This does not prevent molecular gas from cooling to low temperatures provided a sufficient density. Additionally, the gas can also cool adiabatically, which occurs in low density regions behind shocks.

Our model does not incorporate interstellar magnetic fields which may play an important role in molecular cloud dynamics. Nevertheless, recent measurements of the magnetic field strength in molecular clouds show that gravitational forces may exceed those due to magnetic pressure gradients (Crutcher 2012; Crutcher & Kemball 2019). The presence of an interstellar magnetic field could initially increase the supershell’s thickness, thus increasing the timescale for dust grain growth within the supershell (Ferriere et al. 1991).

As already stated, we have not modelled other grain destructive processes that require a shock to kinematically-decouple the gas particles and dust grains, such as kinetic sputtering and grain shattering. However, the superbubble’s interior is very tenuous and thus gas-grain and grain-grain encounters are not very frequent even in the case of large gas-grain and grain-grain relative velocities (see Appendix A.2 in Paper II). This fact, and the fact that sequential supernova shocks soon decay into sound waves within the thermalized superbubble’s interior (Tenorio-Tagle & Bodenheimer 1988), are likely to decrease the relative importance of such processes. In addition, betatron acceleration, which occurs when charged dust grains gyrate along magnetic field lines (Shull 1977), is not likely to play a significant role within the superbubble’s interior given that at high temperatures ($\gtrsim 2 \times 10^5 \text{ K}$), dust grains tend to be neutral (McKee et al. 1987).

7. CONCLUDING REMARKS

By conducting 3-D hydrodynamical simulations, we have explored the early ($\sim 3.2 \text{ Myr}$) evolution of a starburst-driven superbubble and the onset of PISNe in a low-metallicity ($Z = 0.02 Z_\odot$), clumpy molecular cloud. Our main purposes were to study the process of dust grain growth at low-metallicities and the fate of dust grains condensed from the ejecta of pair-instability and core-collapse supernovae. The star cluster’s mechanical feedback has been modeled using the state-of-the-art BOOST stellar model grids (Szécsi et al. 2020) and the SYNSTARS stellar population synthesis code (Franek et al.

2021).

Dense clumps, that randomly move in the gravitational potential well, coalesce and mix with the interclump matter. At the same time, the hot gas that fills the superbubble’s cavity flows through the channels in between overdensities, to then create a net of interconnected shells. It was found that the mixing of clump-interclump material acts as a trigger for an important enhancement (at a rate $\sim 4.8 \times 10^{-5} M_\odot \text{ yr}^{-1}$ during the first 2.5 Myr of the superbubble evolution) of the dust mass in the filamentary/clumpy molecular cloud and the supershell. Around $\sim 2.5 \text{ Myr}$ of the superbubble evolution, the most massive stars in the central star cluster start to explode as PISNe. Their forward shocks move into the shock-heated, low-density cavity, and soon they decay to sound waves (Tenorio-Tagle & Bodenheimer 1988). This behavior might inhibit the destruction of the ejecta-condensed dust grains via non-thermal, shock-induced dust grain disruptive processes. Overall, ~ 13 and ~ 32 per cent of the dust masses injected by PISNe and core-collapse supernovae, respectively, survive even after being processed in multiple supernova collisions, with net dust injection rates of the order $10^{-4} M_\odot \text{ yr}^{-1}$ and $5.4 \times 10^{-5} M_\odot \text{ yr}^{-1}$, respectively. The destruction of dust grains locked-up in the shell is also largely inhibited as the multiple supernova blast waves are marginally transmitted into the supershell; a result originally presented in Paper II.

The net dust contribution by supernovae alone is sufficient to explain the large dust mass present in the gravitationally-lensed galaxy A2744_YD4 (at a redshift $z \sim 8.38$) reported by Laporte et al. (2017), without the need to invoke a top-heavy IMF.

We thus have demonstrated that the processes of dust grain growth and dust injection by supernovae are both efficient pathways that lead to massive amounts of dust to be present in low-metallicity environments populated by young stellar clusters.

8. ACKNOWLEDGEMENTS

This study was supported by CONACYT-México research grant A1-S-28458. S.M.-G. also acknowledges support by CONACYT through project n.482 of the “Programa Investigadoras e Investigadores por México”. The authors thankfully acknowledge the computer resources, technical expertise and support provided by the Laboratorio Nacional de Supercómputo del Sureste de México, CONACYT member of the network of national laboratories, and by the Laboratorio Nacional de Cómputo de Alto Desempeño (LANCAD), project 13-2021. R.W. & J.P. acknowledge financial support from the Czech Science Foundation project No. 19-15008S and by the Astronomical Institute of the Czech Academy of Sciences through the project RVO:67985815. D.Sz. has been supported by the Alexander von Humboldt Foundation. The authors thank the anonymous Referee for a careful reading and helpful suggestions which greatly improved the paper. *Software:* FLASH v4.3 (Fryxell et al. 2000), Numpy Harris et al. (2020), Wind (Wünsch et al. 2017), TreRay (Wünsch & WÜNSCH et al. 2018), CINDER (Martínez-González et al. 2018).

REFERENCES

- Alūzas, R., Pittard, J. M., Hartquist, T. W., Falle, S. A. E. G., & Langton, R. 2012, *MNRAS*, 425, 2212
- Asano, R. S., Takeuchi, T. T., Hirashita, H., & Nozawa, T. 2013, *MNRAS*, 432, 637
- Behrens, C., Pallottini, A., Ferrara, A., Gallerani, S., & Vallini, L. 2018, *MNRAS*, 477, 552
- Bisnovatyi-Kogan, G. S., & Silich, S. A. 1995, *Reviews of Modern Physics*, 67, 661
- Calura, F., Gilli, R., Vignali, C., et al. 2014, *MNRAS*, 438, 2765
- Calura, F., Pipino, A., & Matteucci, F. 2008, *A&A*, 479, 669
- Cardamone, C., Schawinski, K., Sarzi, M., et al. 2009, *MNRAS*, 399, 1191
- Cherchneff, I. 2010, in *Astronomical Society of the Pacific Conference Series*, Vol. 425, *Hot and Cool: Bridging Gaps in Massive Star Evolution*, ed. C. Leitherer, P. D. Bennett, P. W. Morris, & J. T. Van Loon, 237
- Colella, P., & Woodward, P. R. 1984, *Journal of Computational Physics*, 54, 174
- Consiglio, S. M., Turner, J. L., Beck, S., & Meier, D. S. 2016, *ApJ Lett*, 833, L6
- Crutcher, R. M. 2012, *ARA&A*, 50, 29
- Crutcher, R. M., & Kemball, A. J. 2019, *Frontiers in Astronomy and Space Sciences*, 6, 66
- Dalgarno, A., & McCray, R. A. 1972, *ARA&A*, 10, 375
- Draine, B. T. 2011, *Physics of the Interstellar and Intergalactic Medium*
- Dwarkadas, V. V. 2005, *ApJ*, 630, 892
- Dwarkadas, V. V. 2007, *ApJ*, 667, 226
- Dwek, E. 1998, *ApJ*, 501, 643
- Dwek, E., & Cherchneff, I. 2011, *ApJ*, 727, 63
- Elmegreen, B. G. 1988, *Astrophysical Letters and Communications*, 26, 207
- Ferrara, A., Viti, S., & Ceccarelli, C. 2016, *MNRAS*, 463, L112
- Ferriere, K. M., Mac Low, M.-M., & Zweibel, E. G. 1991, *ApJ*, 375, 239
- Fowler, W. A., & Hoyle, F. 1964, *ApJ*, 9, 201
- Franco, J., Tenorio-Tagle, G., Bodenheimer, P., & Rozyczka, M. 1991, *PASP*, 103, 803
- Franeck, A., Wünsch, R., Martínez-González, S., et al. 2021, *ApJ*, submitted
- Fryxell, B., Olson, K., Ricker, P., et al. 2000, *ApJ*, 131, 273
- Gall, C., & Hjorth, J. 2018, *ApJ*, 868, 62
- Gall, C., Hjorth, J., & Andersen, A. C. 2011, *A&A Rev.*, 19, 43
- Haid, S., Walch, S., Naab, T., et al. 2016, *MNRAS*, 460, 2962
- Harris, C. R., Millman, K. J., van der Walt, S. J., et al. 2020, *Nature*, 585, 357
- Indebetouw, R., Matsuura, M., Dwek, E., et al. 2014, *ApJ Lett*, 782, L2
- Jiménez, S., Tenorio-Tagle, G., & Silich, S. 2021, *MNRAS*, 505, 4669
- Kirchschlager, F., Barlow, M. J., & Schmidt, F. D. 2020, *ApJ*, 893, 70
- Koo, B.-C., & McKee, C. F. 1992, *ApJ*, 388, 93
- Koyama, H., & Inutsuka, S.-i. 2002, *ApJ Lett*, 564, L97
- Kozyreva, A., Blinnikov, S., Langer, N., & Yoon, S. C. 2014, *A&A*, 565, A70
- Kroupa, P. 2001, *MNRAS*, 322, 231
- Lada, C. J., & Lada, E. A. 2003, *ARA&A*, 41, 57
- Lancaster, L., Ostriker, E. C., Kim, J.-G., & Kim, C.-G. 2021a, *ApJ*, 914, 89
- Lancaster, L., Ostriker, E. C., Kim, J.-G., & Kim, C.-G. 2021b, *ApJ*, 914, 90
- Laporte, N., Ellis, R. S., Boone, F., et al. 2017, *ApJ Lett*, 837, L21
- Lau, R. M., Hankins, M. J., Kasliwal, M. M., et al. 2021, *ApJ*, 909, 113
- Leśniowska, A., & Michałowski, M. J. 2019, *A&A*, 624, L13
- Lucas, W. E., Bonnell, I. A., & Dale, J. E. 2020, *MNRAS*, 493, 4700
- Mac Low, M.-M., & McCray, R. 1988, *ApJ*, 324, 776
- Martínez-González, S., Silich, S., & Tenorio-Tagle, G. 2021, *MNRAS*, 507, 1175
- Martínez-González, S., Tenorio-Tagle, G., & Silich, S. 2016, *ApJ*, 816, 39
- Martínez-González, S., Wünsch, R., & Palouš, J. 2017, *ApJ*, 843, 95
- Martínez-González, S., Wünsch, R., Palouš, J., et al. 2018, *ApJ*, 866, 40
- Martínez-González, S., Wünsch, R., Silich, S., et al. 2019, *ApJ*, 887, 198
- Mattsson, L., Gomez, H. L., Andersen, A. C., & Matsuura, M. 2015, *MNRAS*, 449, 4079
- McKee, C. F., Hollenbach, D. J., Seab, G. C., & Tielens, A. G. G. M. 1987, *ApJ*, 318, 674
- McLeod, A. F., Ali, A. A., Chevance, M., et al. 2021, *MNRAS*, arXiv:2109.08703
- Michałowski, M. J., Watson, D., & Hjorth, J. 2010, *ApJ*, 712, 942
- Micheva, G., Oey, M. S., Jaskot, A. E., & James, B. L. 2017, *ApJ*, 845, 165
- Nieuwenhuijzen, H., & de Jager, C. 1990, *A&A*, 231, 134
- Nozawa, T., Kozasa, T., & Nomoto, K. 2012, *ApJ Lett*, 756, L35
- Nozawa, T., Kozasa, T., Umeda, H., Maeda, K., & Nomoto, K. 2003, *ApJ*, 598, 785
- Palouš, J., Wünsch, R., Martínez-González, S., et al. 2013, *ApJ*, 772, 128
- Portegies Zwart, S. F., McMillan, S. L. W., & Gieles, M. 2010, *ARA&A*, 48, 431
- Priestley, F. D., Chawner, H., Matsuura, M., et al. 2021, *MNRAS*, 500, 2543
- Relaño, M., Kennicutt, R., Lisenfeld, U., et al. 2016, *A&A*, 595, A43
- Reynolds, D. R., Gardner, D. J., Balos, C. J., & Woodward, C. S. 2019, arXiv e-prints, arXiv:1909.12966
- Rogers, H., & Pittard, J. M. 2013, *MNRAS*, 431, 1337
- Różyczka, M., Tenorio-Tagle, G., Franco, J., & Bodenheimer, P. 1993, *MNRAS*, 261, 674
- Schure, K. M., Kosenko, D., Kaastra, J. S., Keppens, R., & Vink, J. 2009, *A&A*, 508, 751
- Shull, J. M. 1977, *ApJ*, 215, 805
- Smith, B. D., Bryan, G. L., Glover, S. C. O., et al. 2017, *MNRAS*, 466, 2217
- Spitzer, L. 1978, *Physical processes in the interstellar medium*, doi:10.1002/9783527617722
- Svoboda, J., Douma, V., Orlitová, I., & Ehle, M. 2019, *ApJ*, 880, 144
- Szécsi, D., Langer, N., Yoon, S.-C., et al. 2015, *A&A*, 581, A15
- Szécsi, D., & Wünsch, R. 2019, *ApJ*, 871, 20
- Szécsi, D., Wünsch, R., Agrawal, P., & Langer, N. 2020, arXiv e-prints, arXiv:2004.08203
- Taylor, R., Wünsch, R., & Palouš, J. 2018, *MNRAS*, 479, 377
- Tenorio-Tagle, G. 2002, in *Revista Mexicana de Astronomía y Astrofísica Conference Series*, Vol. 12, *Revista Mexicana de Astronomía y Astrofísica Conference Series*, ed. W. J. Henney, J. Franco, & M. Martos, 50–55
- Tenorio-Tagle, G., & Bodenheimer, P. 1988, *ARA&A*, 26, 145
- Tenorio-Tagle, G., Bodenheimer, P., Franco, J., & Rozyczka, M. 1990, *MNRAS*, 244, 563
- Tenorio-Tagle, G., Muñoz-Tuñón, C., Pérez, E., Silich, S., & Telles, E. 2006, *ApJ*, 643, 186
- Tenorio-Tagle, G., Muñoz-Tuñón, C., Silich, S., & Cassisi, S. 2015, *ApJ Lett*, 814, L8
- Tenorio-Tagle, G., Rozyczka, M., Franco, J., & Bodenheimer, P. 1991, *MNRAS*, 251, 318
- Todini, P., & Ferrara, A. 2001, *MNRAS*, 325, 726
- Valentini, M., & Brighenti, F. 2015, *MNRAS*, 448, 1979
- Valiante, R., Schneider, R., Bianchi, S., & Andersen, A. C. 2009, *MNRAS*, 397, 1661
- van Marle, A. J., Meliani, Z., & Marcowith, A. 2015, *A&A*, 584, A49
- Vink, J. S., de Koter, A., & Lamers, H. J. G. L. M. 2000, *A&A*, 362, 295
- Vink, J. S., de Koter, A., & Lamers, H. J. G. L. M. 2001, *A&A*, 369, 574
- Weaver, R., McCray, R., Castor, J., Shapiro, P., & Moore, R. 1977, *ApJ*, 218, 377
- Wünsch, R., Palouš, J., Tenorio-Tagle, G., & Ehlerová, S. 2017, *ApJ*, 835, 60
- Wünsch, R., Walch, S., Dinbier, F., & Whitworth, A. 2018, *MNRAS*, 475, 3393
- Zhukovska, S., Gail, H. P., & Tieloff, M. 2008, *A&A*, 479, 453